# Generalized Morphological Component Analysis for Hyperspectral Unmixing

Xiang Xu, *Member, IEEE*, Jun Li, *Senior Member, IEEE*, Shutao Li, *Fellow, IEEE*, and Antonio Plaza, *Fellow, IEEE*

***Abstract*— Hyperspectral unmixing (HU) is an active research topic in the remote-sensing community. It aims at modeling mixed pixels using a collection of pure constituent materials (*endmembers*) weighted by their corresponding fractional abundances. Among existing unmixing schemes, nonnegative matrix factorization (NMF) has drawn significant attention due to its unsupervised nature, as well as its capacity to obtain both endmembers and fractional abundances simultaneously. In this article, we present a new blind unmixing method based on the generalized morphological component analysis (GMCA) framework, in which an additional constraint is introduced into the standard NMF model to represent the sparsity and morphological diversity of the abundance maps associated with each endmember. More specifically, we take into account the fact that different ground categories in a hyperspectral scene generally exhibit various spatial distributions and morphological characteristics. As a result, when providing a specific dictionary basis for these categories, their corresponding abundance maps (referred to as *sources*) can be sparsely represented. In addition, due to the low correlation between different sources, their sparse representations will not share the same most significant coefficients. With this observation in mind, we can further promote source discrimination and separation in the unmixing process. Moreover, in order to obtain a stable solution of the involved optimization problem, we adopt an alternate iterative constrained algorithm with a threshold descent strategy. Our experiments, carried out on both synthetic and real hyperspectral scenes, reveal that our newly developed GMCA-based unmixing method obtains very promising results with fast convergence speed and requiring significantly less parameter tuning. This confirms the advantage of the proposed spatial morphological component approach for HU purposes.**

***Index Terms*— Blind source separation (BSS), generalized morphological component analysis (GMCA), hyperspectral unmixing (HU), nonnegative matrix factorization (NMF).**

## I. Introduction

HYPERSPECTRAL sensors are able to capture ground remote-sensing signals with very fine spectral resolution, thus promoting the development of quantitative remote sensing applications [1]–[4]. However, due to their limited spatial resolution (as well as the complex distribution of ground categories), the resulting images often contain a large number of mixed pixels [5], [6]. In order to reveal the intrinsic material composition of mixed pixels and adequately exploit hyperspectral imagery (HSI), hyperspectral unmixing (HU) has been an emerging strategy to characterize this kind of remotely sensed data.

Over the past decades, plenty of HU methods have been developed. According to their characteristics, these methods can be divided into two main groups. One group of methods usually adopts a successive processing chain with two separate steps: 1) identify the endmember signatures and 2) estimate their corresponding fractional abundances based on the considered mixing model (e.g., linear mixing model (LMM) or nonlinear mixing model (NLMM) [7], [8]). A category of methods within this group was developed by relying on the pure pixel assumption, including endmember identification methods such as orthogonal subspace projection (OSP) [9], pixel purity index (PPI) [10], N-FINDR [11], vertex component analysis (VCA) [12], among many others [5]. Actually, pure pixels are seldom presented in real HSI scenes. To address this issue, another category of methods was developed without the pure pixel assumption, including methods able to identify (virtual) endmember signatures and their corresponding abundances, such as the simplex identification via split augmented Lagrangian (SISAL) [13], the minimum volume spectral analysis (MVSA) [14], among many others [5]. In both cases, it is a challenge to identify realistic endmember signatures directly from the HSI, without prior knowledge. As an alternative, several methods tend to exploit endmember signatures from a previously available

Manuscript received June 3, 2019; revised September 17, 2019; accepted November 25, 2019. Date of publication December 11, 2019; date of current version March 25, 2020. This work was supported in part by the National Natural Science Foundation of China under Grant 61771496, in part by the Guangdong Provincial Natural Science Foundation under Grant 2016A030313254, in part by the National Key Research and Development Program of China under Grant 2017YFB0502900, in part by the Open Research Fund of Key Laboratory of Spectral Imaging Technology, Chinese Academy of Sciences, under Grant LSIT201708D, in part by the Zhongshan City Science and Technology Research Project under Grant 2018B1015, in part by the Junta de Extremadura (Decreto 14/2018, de 6 de febrero, por el que se establecen las bases reguladoras de las ayudas para la realizacion de actividades de investigacion y desarrollotecnologico, de divulgacion y de transferencia de conocimiento por los Grupos de Investigacion de Extremadura, Ref. GR18060), and in part by the European Union's Horizon 2020 research and Innovation Program under Grant 734541 (EOXPOSURE). *(Corresponding author: Jun Li.)*

X. Xu is with the Zhongshan Institute, University of Electronic Science and Technology of China, Zhongshan 528402, China.

J. Li is with the Guangdong Provincial Key Laboratory of Urbanization and Geo-simulation, School of Geography and Planning, Sun Yat-sen University, Guangzhou 510275, China (e-mail: lijun48@mail.sysu.edu.cn).

S. Li is with the College of Electrical and Information Engineering, Hunan University, Changsha 410082, China (e-mail: shutao_li@hnu.edu.cn).

A. Plaza is with the Hyperspectral Computing Laboratory, Department of Technology of Computers and Communications, Escuela Politécnica, University of Extremadura, 10600 Cáceres, Spain.

Color versions of one or more of the figures in this article are available online at http://ieeexplore.ieee.org.

Digital Object Identifier 10.1109/TGRS.2019.2956562

(and potentially very large) spectral library, such as the public United States Geological Survey (USGS) digital spectral library (available online: http://speclab.cr.usgs.gov/spectral-lib.html). Then, the unmixing process amounts at choosing an optimal subset of library endmembers to model each pixel [15]. Although such library endmembers avoid the direct extraction of image endmembers from the HSI, it is important to note that the library endmember signatures usually exhibit inconsistent acquisition conditions compared to the image pixel signatures, and this inconsistency may cause error propagation to the subsequent abundance estimation step. In addition, considering that spectral variability usually exists in real HSI scenes [16], researchers have proposed many new models to incorporate endmember variability in the unmixing process, such as normal compositional model (NCM) [17] and multiple endmember spectral mixture analysis (MESMA) [18].

From the statistical point of view, HU can be treated as a blind source separation (BSS) problem, and this idea brings the application of nonnegative matrix factorization (NMF)-based unmixing [19]. Compared to the aforementioned two-stage processing chain (and whatever the adopted endmember identification method), NMF-based unmixing not only provides a fully unsupervised procedure (without the pure pixel assumption), but is also able to determine the endmembers and corresponding fractional abundances simultaneously. Moreover, NMF naturally introduces nonnegative constraints into the unmixing model, which makes it particularly suitable for HSI unmixing purposes. In this article, we also focus on the HU issues under the NMF framework.

The standard NMF model is nonconvex and exhibits scale indeterminacy. Therefore, considering only nonnegative constraint is not enough to obtain a stable solution. Recently, researchers have introduced a series of additional constraints into the standard NMF formula. Among them, one possible course of action is directed at imposing constraints on the endmembers themselves, while other strategies prefer to impose constraints on the abundances. In addition, the combination of the two aforementioned lines of action are also exploited in some contributions [20].

Concerning the constraints on the endmembers, a common idea is to explore the intrinsic structure of the whole endmember set. From a convex geometry point of view, a minimum simplex volume constraint can be imposed on the endmember set, leading to a new MVC-NMF [21] unmixing method. Considering the nonconvexity and computational burden of the simplex volume, as well as the fact that a minimum volume simplex is, in essence, equal to a simplex which is as compact as possible, a MDC-NMF [22] method has been proposed, in which an *endmember distance* is designed to measure compactness. Beyond that, and motivated by the smooth changes in spectral wavelength, a smoothness constraint has also been imposed on each endmember signature [23]. However, as the noisy and water-vapor absorption bands are removed, the uniform smoothness is undermined, while the piecewise smoothness actually happens in spectral space [24].

Concerning the constraints imposed on the abundances, since only a few endmembers normally participate in each mixed pixel, the sparsity is reflected on the abundance matrix [24]–[29]. Besides, the unmixing can be treated as a rank reduction procedure, where the high spatial correlation is translated into the low rank of the involved abundance matrix, so the low-rank constraint can also be applied for this purpose [30]–[32]. Last but not least, many kinds of spatial constraints have been applied in abundance estimation, highlighting some spatial and/or structural characteristics such as local homogeneity, morphological diversity, etc. [33]. Among them, sparse constraints are the most widely adopted, and different sparse-inducing representation patterns have been considered. On the one hand, as the abundance maps of each endmember show a localized distribution, it is possible to enhance row sparsity on the abundance matrix. With this observation, Jia and Qian [24] designed a quantitative sparse measurement by using a division between the $\ell_1$ and $\ell_2$ norm on each row of the abundance matrix, so as to evaluate the energy concentration of all components in the vector. However, this model needs to know the sparseness degree of the abundances in advance, thus bringing some uncertainty to the final unmixing results. In [26], a novel sparsity measure (namely, *S-measure*) was designed based on the higher order norms of the abundance vector, which does not need an exact sparseness degree. On the other hand, due to the fact that normally only a few endmembers contribute to one single mixed pixel, the sparse representation can be implemented on each column of the abundance matrix. Initially, the $\ell_0$ and $\ell_1$ norms are commonly adopted, but $\ell_0$ norm is NP-Hard, while $\ell_1$ norm cannot enforce further sparsity when the full additivity constraint is imposed on the estimated abundances. After, an unbiased $\ell_{1/2}$ norm constraint is incorporated into the NMF model [34], which provides sparser and more accurate unmixing results than those delivered with the $\ell_1$ norm [25]. Moreover, if an over-complete endmember library is adopted, a collaborative sparsity constraint can also be adopted, in which case an $\ell_{2,1}$ mixed-norm is imposed to promote row sparsity on the abundance matrix [27]. It should be noted that the aforementioned $\ell_p$ (for $0 \leq p < 1$) norm constraints are non-continuous and non-differentiable, leading to the numerical instability and noise interference in the optimization process. To address this issue, in [35], an arctan function with Lipschitz continuous characteristic is introduced to exploit sparsity of the abundances, thus enhancing the numerical stability and the immunity to noise corruption. Recently, a superpixel-based group-sparsity constraint has also been developed [36], in which a modified mixed-norm was designed to exploit the shared sparsity pattern of each superpixel. This idea can be seen as an integration of the spatial structure and the sparsity of the abundances. As discussed above, the solution of a sparse constrained NMF model relies heavily on the initial selection and the regularization parameters, hence in several cases the unmixing results are undetermined.

Relatively speaking, imposing spatial structural constraints on the abundance images (e.g., piecewise smoothness and local manifold) often acts as a supplement for the sparse constraints. Considering that neighboring pixels are more likely to have similar fractional abundances for the same endmember, abundance smoothness constraints have also been

combined with the NMF model [37]. Based on the fact that spectral signatures of neighborhood pixels still exhibit certain differences, a more refined local smoothness constraint was developed in [38]. In [28], total variation (TV) regularization is introduced to capture the piecewise smoothness structure of the abundance matrix. In addition to the aforementioned smoothness constraints, manifold structures have also been incorporated into the sparse constrained NMF formula [39]–[44]. In these methods, a graph model (e.g., single graph, multiple graphs, and hypergraph) is established to enhance the local affinity structure between neighboring pixels. In order to fully exploit the structural characteristics of abundance images, in [45] the HSI was segmented into a series of small homogeneous regions by using the graph cut technique, and then the consistent data distributions within each region are explored while discriminating different data structures across regions. In [33], the HSI was segmented into homogeneous regions and detailed regions. For the homogeneous regions, sparse constraint was adopted, whereas for the detailed regions, a graph regularized semi-NMF was performed.

Furthermore, researchers have incorporated the deep learning into the NMF model and proposed a deep NMF structure for exploring hierarchical features in the unmixing process [46], [47]. Generally, in each layer, the abundance matrix is directly decomposed into the abundance matrix and endmember matrix of the next layer. Then, the aforementioned sparse constraints or manifold structural constraints are imposed on the abundance matrix of each layer.

As a summary, although the sparse and structural constraints bring more well-posed NMF models, some important issues deserve further exploration. First, most spatial structure constraints are designed based on the spectral similarity between neighboring pixels, which is insufficient for characterizing some high-level structure attributes, including spatial distribution, morphology, etc. Compared to neighborhood similarity, these high-level spatial attributes can significantly enhance source representation and discrimination. Second, in most existing constrained-NMF models, the complementarity between the sparse and structure constraints is not sufficiently explored (specifically, the beneficial effects of spatial structure information on sparse representation have not been fully explored). Last but not least, the involved optimization problems in most existing constrained-NMF models are difficult to solve and the corresponding solutions are often unstable. As a result, it is necessary to provide more efficient and stable optimization algorithms.

In this article, we present a new unsupervised HU method based on the generalized morphological component analysis (GMCA) framework [48], [49]. The core idea of GMCA is to adopt two kinds of priors: sparsity and morphological diversity. More specifically, different ground categories in the HSI generally exhibit various geometrical structures or morphologies, as well as diverse spatial distributions. When providing a specific dictionary basis, their corresponding abundance maps (or *sources*) can be sparsely represented, and if the correlation between sources is low, their sparse representations will not share the same most significant coefficients, thus promoting source discrimination and separation. Compared with state-of-the-art NMF-based unmixing methods, the main innovative contributions of our work can be summarized as follows.

1) We introduce a new sparse-constrained NMF formula. Here, the sparsity comes from the sparse representation of morphological components, which are decomposed from each source in the image.
2) We exploit the morphological diversity between the abundance maps of each endmember and their benefits in terms of sparse representation and source separation, while most conventional constrained NMF schemes treat the sparsity and spatial structure constraints in a relatively independent way.
3) We adopt an alternative iteration constrained algorithm with a threshold descent strategy to solve the involved optimization problem. Here, the threshold descent strategy can identify the mixing directions by means of searching the largest coefficients and refining them afterward. Thus, a global optimal solution can be obtained.

Our experiments, carried out on both synthetic and real HSI scenes, reveal that the proposed GMCA-based unmixing method leads to very promising results, as well as fast convergence speed and significantly less parameter tuning. This confirms the advantages of spatial morphological component analysis (MCA) for HU purposes.

The remainder of this article is organized as follows. Section II details the proposed GMCA-based unmixing method, as well as the corresponding optimization algorithm. Sections III and IV discuss our experimental results, obtained by using both synthetic and real HSI scenes, and provide comprehensive performance assessments and comparisons with some state-of-the-art unmixing methods. Section V concludes this article with some remarks and hints at plausible future research lines.

## II. GMCA-Based HU Method

In this section, the LMM is first briefly introduced. Then, the standard NMF model and two main optimization algorithms are discussed. Next, the newly proposed GMCA-based unmixing model is detailed, and the advantages of GMCA in terms of source separation are discussed. Finally, the solution of the involved optimization problem is presented and discussed.

### A. LMM

In our proposed unmixing scheme, the LMM is adopted due to its simplicity as well as its capacity to provide an approximate description of light scattering occurring in real scenes [5]. For a given pixel vector $\mathbf{x} = [x_1, \ldots, x_b]^T$, with $b$ denoting the number of spectral channels, the LMM can be expressed as

$$\mathbf{x} = \mathbf{M}\mathbf{s} + \mathbf{n} \tag{1}$$

where $\mathbf{M} = [\mathbf{m}_1, \ldots, \mathbf{m}_p] \in \mathbb{R}^{b \times p}$ is the endmember signatures matrix, $\mathbf{s} = [s_1, \ldots, s_p]^T$ is the abundance vector of pixel, $p$ is the number of endmembers, and $\mathbf{n}$ accounts for the additive noise and model imperfections. Generally, the abundance vector of a pixel meets two constraints: the abundance

nonnegativity constraint (ANC) (i.e., $s_i \geq 0$), and the abundance sum-to-one constraint (ASC) (i.e., $\sum_{i=1}^{p} s_i = 1$), respectively [50]. Under the LMM, and given a HSI, the purpose of unsupervised unmixing is to recover the endmember signatures matrix, along with the corresponding fractional abundances matrix.

### B. Standard NMF Model

As a widely used unsupervised unmixing model, the standard NMF model adopts a similar formula as the aforementioned LMM. However, from the perspective of BSS, the NMF assumes that the observed original HSI is a linear instantaneous mixture of unknown sources (corresponding to each row vector in the abundance matrix of the LMM) with an unknown mixing matrix (corresponding to the endmember matrix in the LMM). Here, we present the standard NMF model as

$$\mathbf{Y} = \mathbf{MS} + \mathbf{N} \tag{2}$$

where $\mathbf{Y} = [\mathbf{y}_1^T, \ldots, \mathbf{y}_b^T]^T$ is the $b \times t$ matrix, in which each row stands for a single-channel image $\mathbf{y}_i$ $(i = 1, \ldots, b)$ with $t$ number of pixels, and $\mathbf{S} = [\mathbf{s}_1^T, \ldots, \mathbf{s}_p^T]^T$ is the source matrix whose rows $\mathbf{s}_j$ $(j = 1, \ldots, p)$ are the sources that denote the abundance maps of each endmember. Finally, the matrix $\mathbf{N} \in \mathbb{R}^{b \times t}$ is added to account for noise or model imperfections. Obviously, (2) can be treated as a matrix form of (1).

In order to solve (2) by using the NMF algorithm, the noise $\mathbf{N}$ is usually assumed to be independent and identically distributed Gaussian noise. Then, the objective function based on the maximum-likelihood estimation is presented as follows:

$$\begin{aligned} &\arg\min_{\mathbf{M},\mathbf{S}} \frac{1}{2}\left\|\mathbf{Y} - \mathbf{MS}\right\|_F^2 \\ &\text{s.t. } \mathbf{M} \geq 0, \quad \mathbf{S} \geq 0, \;\; 1_p^T \mathbf{S} = 1_t^T \end{aligned} \tag{3}$$

where the notation $\|\cdot\|_F$ is the Frobenius norm, $1_p$ and $1_t$ are all one column vectors of size $p$ and $t$. Considering that the problem (3) is non-convex, while the two subproblems corresponding to $\mathbf{M}$ and $\mathbf{S}$ are convex, the former is generally solved by alternately updating $\mathbf{M}$ and $\mathbf{S}$.

A well-known type of optimization algorithm is the fixed-point algorithm, which adopts a multiplicative update strategy to minimize problem (3). Among others, Lee and Seung [51] developed a weighted gradient descent method to alternately update $\mathbf{M}$ and $\mathbf{S}$ at each iteration, in which the weights are designed to keep the cost function monotonically decreasing as well as maintaining the positivity of $\mathbf{M}$ and $\mathbf{S}$ for all iterations. In this case, the update rules of $\mathbf{M}$ and $\mathbf{S}$ are

$$\hat{\mathbf{M}} \leftarrow \mathbf{M} \odot (\mathbf{YS}^T) \oslash (\mathbf{MSS}^T + \varepsilon) \tag{4}$$

$$\hat{\mathbf{S}} \leftarrow \mathbf{S} \odot (\mathbf{M}^T\mathbf{Y}) \oslash (\mathbf{M}^T\mathbf{MS} + \varepsilon) \tag{5}$$

where $\odot$ and $\oslash$ denote the element-wise matrix multiplication and division operators, respectively, and $\varepsilon$ is a small regularization applied to the denominator in order to avoid dividing by zero. The multiplicative update algorithm is considered as a standard NMF optimization algorithm due to the fact that it does not require parameter tuning. However, it is too slow in practice, and even hard to converge to a local minimum [52].

Another type of optimization algorithms that can be used for solving problem (3) is called alternative nonnegative least squares (ANLS) [53], [54], in which the pseudo-inverse is calculated in each subproblem, and then the corresponding results are projected onto the positive quadrant to satisfy the nonnegative constraint. In this case, the iterative update rules of $\mathbf{M}$ and $\mathbf{S}$ are expressed in the following equation:

$$\hat{\mathbf{M}} \leftarrow [\mathbf{YS}^T(\mathbf{SS}^T)^{-1}]_+ \tag{6}$$

$$\hat{\mathbf{S}} \leftarrow [(\mathbf{M}^T\mathbf{M})^{-1}\mathbf{M}^T\mathbf{Y}]_+ \tag{7}$$

where the notation $[x]_+ = \max(x, 0)$ denotes a positive projection operation. Similar to the multiplicative update algorithm, ANLS also owns a very simple and efficient implementation process. However, the ANLS only applies to the least square cost function, and the convergence of the algorithm is still not guaranteed.

### C. GMCA-Based Unmixing

As stated previously, only imposing nonnegative constraints on the NMF model is generally insufficient. To this end, we introduce the GMCA in this article for HSI unmixing purposes. The GMCA model is based on the priors of sparsity and morphological diversity, which offers a generalization of the MCA [55], [56]. In the MCA framework, the original image is assumed to be a linear combination of multiple morphological components (e.g., piecewise smoothness and texture components), where each morphological component can be sparsely represented under a specified dictionary basis, and this dictionary will not provide sparse representation for the other morphological components. The GMCA framework further extends MCA framework and applies it to a BSS context. According to (2), GMCA assumes that the original image $\mathbf{Y}$ is a linear instantaneous mixture of multiple unknown sources $\mathbf{S}$, along with an unknown mixing matrix $\mathbf{M}$. Moreover, each source $\mathbf{s}_j$ $(j = 1, \ldots, p)$ can be modeled as a linear combination of multiple morphological components, in which each component can be sparsely represented by its associated dictionary basis as expressed in the following equation:

$$\mathbf{s}_j \approx \sum_{k=1}^{K} \mathbf{s}_{jk} = \sum_{k=1}^{K} \mathbf{D}_k \alpha_{jk} \tag{8}$$

where $K$ is the number of morphological components contributed to one single source, $\mathbf{s}_{jk}$ is the $k$th morphological component corresponding to the source $\mathbf{s}_j$, and $\alpha_{jk}$ is the sparse representation coefficient vector of the morphological component $\mathbf{s}_{jk}$ under the dictionary $\mathbf{D}_k$. Also $\mathbf{D} := (\mathbf{D}_1, \ldots, \mathbf{D}_K)$ is built as a concatenated dictionary, which acts as a discriminator between different morphological components, selecting one component over the others. Following the assumptions of sparsity and morphological diversity, each source can be represented with only a few most significant representation coefficients, while other coefficients are small, or close to zero. Moreover, the most significant coefficients between different sources will show inconsistence due to their

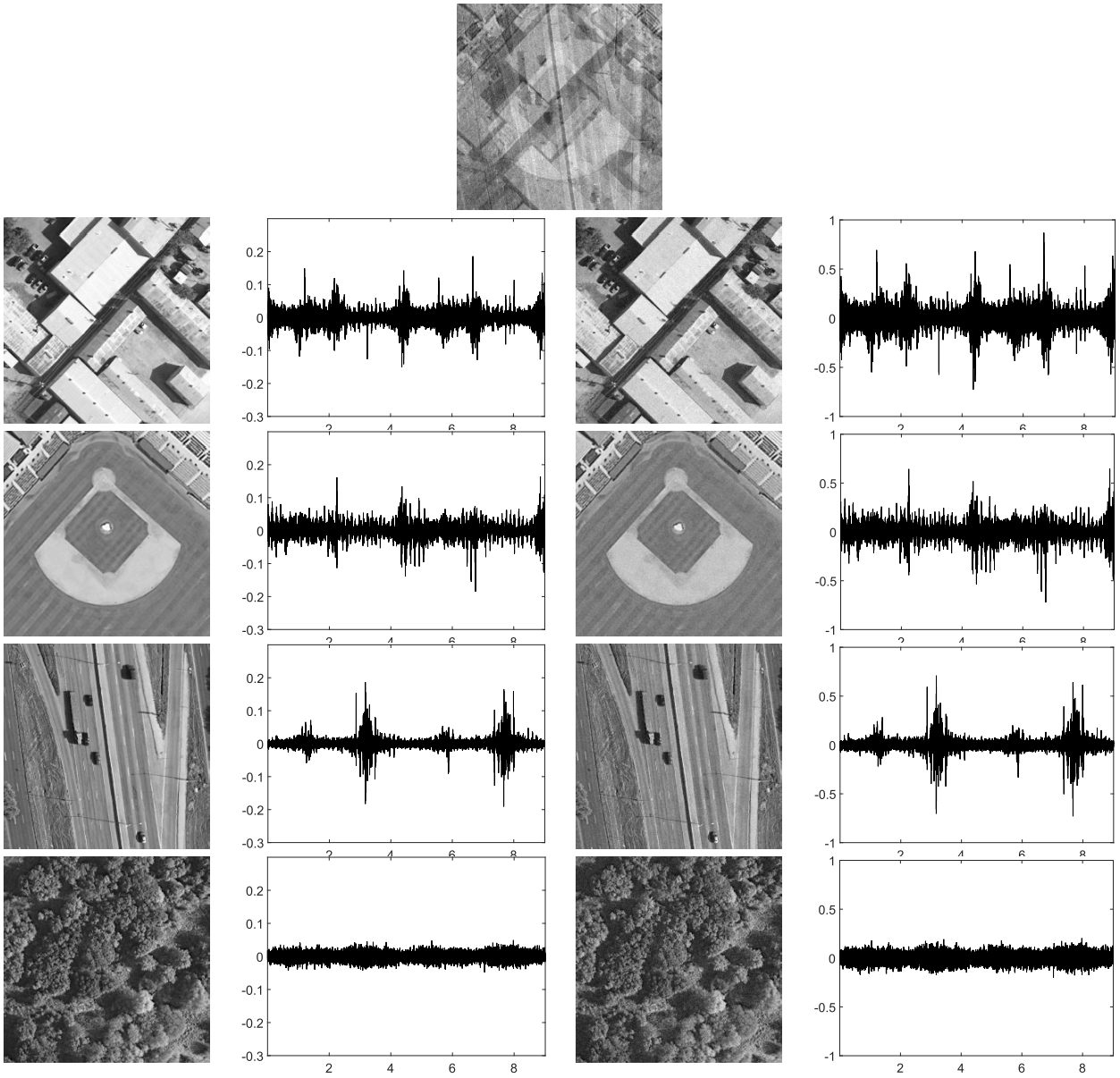

Fig. 1. Toy example: GMCA for BSS. The first row shows one channel image of the mixed images, the first and second columns show the real source images with the corresponding Curvelet transform coefficients (only the coefficients of the fourth scale layer are presented), the third and fourth columns show the estimated sources with the corresponding Curvelet transform coefficients.

morphological diversity. This is a critical issue for the success of source separation process. Finally, GMCA seeks an unmixing scheme by estimating the mixing matrix $\mathbf{M}$, leading to the sparsest sources $\mathbf{S}$ in the concatenated dictionary $\mathbf{D}$. The involved constrained optimization problem is given by

$$\arg\min_{\mathbf{M},\alpha} \frac{1}{2}\left\|\mathbf{Y}-\mathbf{MD}\alpha\right\|_F^2 + \lambda \sum_{j=1}^{p}\sum_{k=1}^{K} \|\alpha_{jk}\|_1. \tag{9}$$

Here, in order to support the efficiency of the GMCA-based unmixing scheme, we provide a toy experiment to illustrate the way GMCA exploits sparsity and morphological diversity. First, four remote-sensing images with the same size of $256 \times 256$, including building, baseball diamond, freeway, and forest, are chosen and converted into grayscale images. Then, these grayscale images are mixed to form a composite image data with 50 channels, where each channel is a linear random mixture of the above four grayscale images. In order to better demonstrate the robustness to noise, Gaussian noise with signal-to-noise ratio (SNR) of 10 dB is added to the composite image, so as to form the final test image. The first row in Fig. 1 shows one channel image of the mixed images, and the first column shows four real grayscale source images. It can be observed that these specially chosen images show different scene information respectively, thus reflecting distinct morphological characteristics, namely, satisfying morphological diversity. Moreover, to obtain a sparse representation of these source images, we adopt the Curvelet transform to construct dictionary (due to its anisotropy, which is very beneficial to characterize the image edges). In this case, we used a fast

discrete Curvelet transform provided from a CurveLab software package [57], which is based on the unequally spaced fast Fourier transform (USFFT), and the number of scales including the coarsest wavelet level is set to $\log_2(N)-3$, where $N$ is the maximum of width and height of image. As a result, five number of scales transformed coefficients are obtained. The second column of Fig. 1 shows the Curvelet coefficients corresponding to the real source images (here only the coefficients of the fourth scale layer are presented). It can be observed that, in such well-chosen Curvelet transform domain, different sources show most significant diverse coefficients (except for the "forest" image, in which very few significant coefficients exist), thus satisfying sparsity and morphological diversity.

After that, the GMCA is performed on the mixed images for source separation purpose, and the estimated sources as well as the corresponding Curvelet transform coefficients are shown in the third and fourth columns of Fig. 1. Obviously, the GMCA not only keeps the similar sparsity divergence with respect to the real sources but also enhances and concentrates the significant sparse coefficients in the estimated sources. Therefore, if the sources are not too correlated, it can be attributed to the enhancement of separability by the morphological diversity, which means that these sources (with different morphological characteristics) are diversely sparse, and sparser sources lead to more separability. In addition, as a sparsity-based algorithm, GMCA demonstrates to be very robust to noise. This is due to the fact that a sparse source generally has few significant coefficients in the sparse domain, while the noise is typically not sparse, so it is easier to separate noise from the sources in such domain.

Equation (9) is the standard GMCA formula, in which the sparse constraint is imposed on the coefficient vectors of each source image. In this case, the item of $\|\mathbf{Y}-\mathbf{MS}\|_F^2$ is represented in the direct domain, while the item of sparse constraint $\|\alpha\|_1$ is represented in the transformed domain. Two kinds of representation domains exist in one objective formula, leading to a very difficult optimization solution. In order to simplify the optimization solution, as well as considering the characteristics of HSI, we transfer the sparse constraint on the coefficients of the transformed domain into the sparse constraint on the sources of the direct domain and obtain a revised formula is given as

$$\arg\min_{\mathbf{M},\mathbf{S}} \frac{1}{2}\left\|\mathbf{Y}-\mathbf{MS}\right\|_F^2+\lambda\sum_{j=1}^{p}\|\mathbf{s}_j\|_1+i^+(\mathbf{M})+i^+(\mathbf{S}) \tag{10}$$

where $\mathbf{s}_j$ is the $j$th row of matrix $\mathbf{S}$, which represents the abundance map of the $j$th endmember. $i^+(\cdot)$ is a characteristic function to enforce the nonnegative constraint as

$$i^+(x)\mapsto\begin{cases}0, & \text{if } x\geq 0\\ +\infty, & \text{otherwise.}\end{cases} \tag{11}$$

Compared to (9), (10) is not only simpler and more efficient due to the fact that the sparse constraint term and the data fidelity term are all in the direct domain but also can be explained in HSI scenes. On the one hand, the source images obtained by the multiplication of their corresponding sparse coefficient vectors and the concatenated dictionary, generally still show certain sparsity and diversity, which means the most significant entries in each obtained source should be disjoint. On the other hand, different ground categories in HSI scenes generally exhibit various and localized spatial distributions, so the abundance maps corresponding to each endmember possibly show different geometrical structures or morphological characteristics. When imposing sparse constraint on the abundance maps of each endmember, it means that different abundance maps will have disjoint the most significant entries, thus playing an important role for source separation.

To this end, the main innovative contributions of our work is that we introduce a sparsity constraint on the abundance maps corresponding to each endmember, and such row sparsity constraint is derived from the idea of the GMCA framework. Specifically, the sparse constraint in (10) is characterized by using the spatial morphological diversity of different sources, which denote the fact that morphological components in a source exhibit a sparse representation under the specified dictionary basis. When combining all morphological components, these sources will also own sparse representations under the corresponding concatenated dictionary. This idea is crucial for the HSI unmixing scheme, in which the ground categories generally do not share the same spectral signatures and spatial distributions, so their corresponding abundance maps will present some kinds of diversity.

### D. Solution of the Optimization Problem

The optimization problem (10) is not convex because of the product between $\mathbf{M}$ and $\mathbf{S}$, so we split it into two convex subproblems and adopt an alternative iteration constrained solution process. Meanwhile, considering that during the optimization process, the cumulative sum of the sparse constraints on all rows can be simply treated as the sparse constraint on the whole matrix, so the term of $\sum_{j=1}^{p}\|\mathbf{s}_j\|_1$ in (10) is converted into the sparse constraint term of the whole matrix $\mathbf{S}$. Finally, the two split subproblems are

$$\arg\min_{\mathbf{S}} \frac{1}{2}\left\|\mathbf{Y}-\mathbf{MS}\right\|_F^2+\lambda\|\mathbf{S}\|_1+i^+(\mathbf{S}) \tag{12}$$

$$\arg\min_{\mathbf{M}} \frac{1}{2}\left\|\mathbf{Y}-\mathbf{MS}\right\|_F^2+i^+(\mathbf{M}). \tag{13}$$

Now, the above two subproblems are convex, but they are still hard to solve due to their non-smoothness and the fact that the regularization terms in these subproblems are nondifferentiable. Here, in order to obtain a stable solution of the two constrained subproblems, we introduce an exactly alternative optimal process based on the proximal splitting techniques. The idea of proximal splitting techniques is to split a convex (but not differentiable) function into several convex functions, and then perform the alternating optimization. Focusing on (12), it can be divided into two functions: one part is a smooth and differentiable data fidelity term, defined as $f(\mathbf{S})=\frac{1}{2}\|\mathbf{Y}-\mathbf{MS}\|_F^2$, and the other part comprises two nonsmooth and nondifferentiable convex regularization terms, defined as $g(\mathbf{S})=\lambda\|\mathbf{S}\|_1+i^+(\mathbf{S})$. The function $f(\mathbf{S})$ is differentiable, generally the gradient descent algorithm can

be directly adopted to pursuit a local minimum, in this case, the gradient of $f(\mathbf{S})$ can be calculated as $\nabla f(\mathbf{S}) = \mathbf{M}^T(\mathbf{MS} - \mathbf{Y})$, which is $L$-Lipschitz continuous gradient, and $L = \|\mathbf{M}^T\mathbf{M}\|_s$ is the spectral norm of matrix $\mathbf{M}$. As a result, we can solve part-problem $f(\mathbf{S})$ by using the following iterative updating formula:

$$\hat{\mathbf{S}} \leftarrow \mathbf{S} - \frac{1}{L}\nabla f(\mathbf{S}). \tag{14}$$

The function $g(\mathbf{S})$ is not differentiable but convex, which admits an explicit proximal operator with a closed-form expression. Concretely, for the $\ell_1$ norm constraint, the nonnegative soft-thresholding operator is used, as defined in the following equation:

$$[ST_\lambda(\mathbf{S})]_+ \mapsto \ sign(\mathbf{S})[|\mathbf{S}| - \lambda]_+. \tag{15}$$

Here, we introduce a forward-backward splitting (FBS) algorithm [58] to obtain an exactly optimal solution. The iteration procedure of FBS algorithm consists of a forward (explicit) gradient step on $f(\mathbf{S})$, followed by a backward (implicit) step on $g(\mathbf{S})$, this backward step adopts a proximal operator and can also be regarded as a gradient descent step. However, due to the fact that it is performed on the estimated final result, not on the result of the previous iteration, it is called backward step. In this case, the update rule of $\mathbf{S}$ in the subproblem (12) is expressed as

$$\begin{aligned}\hat{\mathbf{S}} &\leftarrow [ST_{\frac{\lambda}{L}}(\mathbf{S} - \frac{1}{L}\nabla f(\mathbf{S}))]_+ \\ &\leftarrow [ST_{\frac{\lambda}{L}}(\mathbf{S} - \frac{1}{L}(\mathbf{M}^T(\mathbf{MS} - \mathbf{Y})))]_+ \\ &\leftarrow [\mathbf{S} - \frac{1}{L}(\mathbf{M}^T(\mathbf{MS} - \mathbf{Y})) - \frac{\lambda}{L}]_+ \\ &\leftarrow [\mathbf{S} - \frac{1}{L}(\mathbf{M}^T(\mathbf{MS} - \mathbf{Y}) - \lambda)]_+. \end{aligned} \tag{16}$$

It should be noted that, as opposed to the traditional thresholding strategy, an iterative soft-thresholding is performed on the gradient (while not directly on the source values).

The solution of subproblem (13) is similar to subproblem (12), which can also be split into two parts: a norm-constrained term $f(\mathbf{M}) = \frac{1}{2}\|\mathbf{Y} - \mathbf{MS}\|_F^2$, and a nonnegative orthant term $g(\mathbf{M}) = i^+(\mathbf{M})$. In this case, the projected gradient algorithm can be directly used, and the corresponding iterative updating formula is shown in the following:

$$\begin{aligned}\hat{\mathbf{M}} &\leftarrow [\mathbf{M} - \frac{1}{L_s}\nabla f(\mathbf{M})]_+ \\ &\leftarrow [\mathbf{M} - \frac{1}{L_s}((\mathbf{MS} - \mathbf{Y})\mathbf{S}^T)]_+ \end{aligned} \tag{17}$$

where $L_s = \|\mathbf{SS}^T\|_s$ is the spectral norm of matrix $\mathbf{S}$.

Moreover, the involved iterative optimization process applies a threshold descent strategy, which has a significant impact on the performance of source separation process. In other words, the threshold $\lambda$ evolves from a large penalization value, and then swiftly decreases to smaller values. This particular decreasing thresholding scheme provides robustness to the algorithm by working first on the most significant features extracted from the data, and then progressively incorporating smaller details to finely tune the model parameters, thus leading to faster convergence (especially in the iterations associated with each subproblem).

To conclude this section, we provide a pseudocode description of the involved optimization process in Algorithm 1. It can be observed that the whole optimization process includes a two-layer iterative process, where the outer layer is alternatively split into $\mathbf{M}$ and $\mathbf{S}$, as well as the threshold descent step, while, for each subproblem, an inner iteration is performed by using the FBS algorithm.

**Algorithm 1** Pseudo Code of the Proposed GMCA-Based HSI Unmixing Method

**Input:**

Original HSI data: $\mathbf{Y}$;
Final threshold computation: $\sigma$.
Maximum number of iterations of outer layer: $max\_it$;
Maximum number of iterations of FBS algorithm: $fbs\_it$.

**Output:**

Endmember matrix $\mathbf{M}$ and Abundance matrix $\mathbf{S}$.

Estimate the number of endmembers $p$ by using HySime [59].
Initialize $\mathbf{M}$ with the first $p$ principal components.
**for** k = 1 to 2 **do**
    // Alternate between ANLS updates and FBS updates.
    $\hat{\mathbf{S}} = [(\mathbf{M}^T\mathbf{M})^{-1}\mathbf{M}^T\mathbf{Y}]_+$;
    $\hat{\mathbf{M}} = [\mathbf{YS}^T(\mathbf{SS}^T)^{-1}]_+$;
    $\hat{\mathbf{S}} = FBS(\mathbf{M}^T\mathbf{Y}, \mathbf{M}^T\mathbf{M}, \mathbf{S}, 0, fbs\_it)$;
    $\hat{\mathbf{M}} = FBS(\mathbf{SY}^T, \mathbf{SS}^T, \mathbf{M}^T, 0, fbs\_it)$;
    $\hat{\mathbf{M}} = \hat{\mathbf{M}}^T$;
**end for**

// Main loop.
$\mathbf{M} = Normalize\_M(\mathbf{M}, \mathbf{S})$.
$\lambda_0 = \|\mathbf{M}^T(\mathbf{MS} - \mathbf{Y})\|_\infty$

**for** i = 1 to $max\_it$ **do**
    ======Update $\mathbf{S}$ when $\mathbf{M}$ fixed======
    $\hat{\mathbf{S}} = FBS(\mathbf{M}^T\mathbf{Y}, \mathbf{M}^T\mathbf{M}, \mathbf{S}, \lambda, fbs\_it)$;
    $\hat{\mathbf{S}} = Normalize\_S(\mathbf{M}, \hat{\mathbf{S}})$.
    ======Update $\mathbf{M}$ when $\mathbf{S}$ fixed======
    $\hat{\mathbf{M}} = FBS(\mathbf{SY}^T, \mathbf{SS}^T, \mathbf{M}^T, 0, fbs\_it)$;
    $\hat{\mathbf{M}} = \hat{\mathbf{M}}^T$;
    $\hat{\mathbf{M}} = Normalize\_M(\hat{\mathbf{M}}, \mathbf{S})$.
    ==========Update $\lambda$==========
    $res\_std = estNoiseStdDev(\mathbf{Y} - \hat{\mathbf{M}}\hat{\mathbf{S}})$;
    $\lambda_{new} = \sigma \times res\_std$;
**end for**

In Algorithm 1, function $FBS()$ is the FBS algorithm used to solve two subproblems iteratively. $Normalize\_M()$ and $Normalize\_S()$ are two regularization functions, which are used to regularize one matrix and then assign the scales to the other matrix. Function $estNoiseStdDev()$ is used to estimate the noise standard deviation of the current residual.

## III. Experiments on Synthetic Data

In this section, a comprehensive experimental assessment based on synthetic HSI data is carried out, as these synthetic data can be fully controlled for evaluating the performance of our newly developed method. At the same time, some state-of-the-art unmixing methods, including VCA + FCLS, MVC-NMF, and R-CoNMF, are chosen for comparison with our proposed GMCA-based HSI unmixing method (referred to hereinafter as GMCA-HU). Among the considered methods, VCA + FCLS is a classical two-step unmixing strategy, in which the VCA algorithm is used for endmember identification and then a fully constrained least squares (FCLS) [50] is used for abundance estimation. MVC-NMF and R-CoNMF are all NMF-based unmixing methods that provide both a set of endmembers and their associated abundances, MVC-NMF imposes minimum volume simplex constraints on the endmember set, whereas R-CoNMF imposes a collaborative row sparsity on the abundance matrix.

In our experiments, two metrics are introduced for quantitative assessment: the first one is the spectral angle distance (SAD), which is defined as the spectral angle between the estimated and ground-truth endmember signatures, as shown in (18). The more the spectral similarity, the smaller the values of SAD. The second one is the root mean square error (RMSE), which is calculated as the difference between the estimated and ground-truth abundances, as shown in (19), in which $t$ denotes the length of the source vector $\hat{\mathbf{s}}$. In this case, since we generate the data synthetically, we can compare the extracted endmembers and the derived abundances with the ground-truth ones used in the simulation of the data

$$\mathrm{SAD}(\hat{\mathbf{m}}, \mathbf{m}) = \cos^{-1}\left(\frac{\hat{\mathbf{m}}^T \mathbf{m}}{(\|\hat{\mathbf{m}}\|)(\|\mathbf{m}\|)}\right) \tag{18}$$

$$\mathrm{RMSE}(\hat{\mathbf{s}}, \mathbf{s}) = \frac{1}{\sqrt{t}}\|\hat{\mathbf{s}} - \mathbf{s}\|_F. \tag{19}$$

The rest of this section is organized as follows. First, the procedure for generating the synthetic HSI data is presented. Then, the experimental settings are reported. After that, detailed discussions of the obtained experimental results are carried out.

### A. Generation of the Synthetic HSI Data

Our synthetic HSI data are generated by adopting a similar procedure with regard to the one adopted in [25]. First, several endmember signatures are randomly picked out from the USGS digital spectral library. The spectral curves of some endmember signatures are shown in Fig. 2. Then, a synthetic HSI with a size of 256 × 256 pixels and 221 bands is segmented into 256 nonoverlapped spatial subblocks with the same spatial size of 16 × 16 pixels. For each subblock, a random endmember signature is initially assigned to all the associated pixels. After that, a spatial low-pass filter is performed on each pixel with a neighborhood window size of 33 × 33, so as to generate mixed pixels as well as locally smooth abundance distributions. It should be noted that, the larger the size of the filter window, the higher the mixture degree of the simulated pixels. Furthermore, in order to remove the pure pixels from the image, the abundance fractions of each pixel

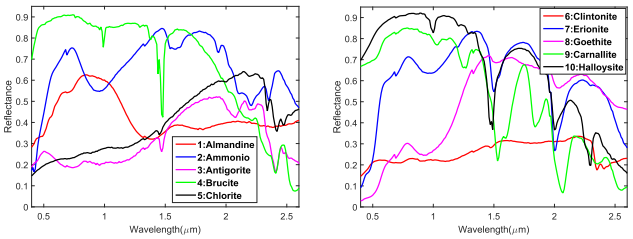


Fig. 2. Some randomly chosen endmember signatures from the USGS library that have been used to generate synthetic data in our experiments.

are thresholded by a parameter $\theta$ ($\theta < 1$); this means that, if the abundance fraction of an endmember in a given pixel is larger than $\theta$, all the abundance fractions of the endmembers in this pixel are set to $1/p$, where $p$ is the number of endmembers used to generate the synthetic HSI. Finally, zero-mean white Gaussian noise is added to generate the noisy synthetic HSI data, in which the SNR is defined as

$$\mathrm{SNR} = 10\log_{10}\left(\frac{E[\mathbf{Y}^T\mathbf{Y}]}{E[\mathbf{N}^T\mathbf{N}]}\right) \tag{20}$$

where $E[\cdot]$ denotes the mathematical expectation.

### B. Experimental Settings

Four experiments have been performed on synthetic HSI data sets in order to account for the following important aspects: 1) noise robustness; 2) sensitivity to the mixture degree of pixels; 3) sensitivity to the number of endmembers; and 4) sensitivity to the parameter $\sigma$. Concerning the noise robustness, we have generated synthetic scenes with different SNRs (10, 30, 50, 70 dB, $+\infty$), in which $+\infty$ means no noise is imposed. Concerning the sensitivity of the method to the mixture degree of pixels, we have considered the values of $\theta$ of (0.6, 0.8) to threshold the abundance fractions of each pixel (the larger the $\theta$ is, the lower the degree of mixture in each pixel). Concerning the sensitivity to the number of endmembers, we have generated synthetic scenes with different numbers of endmembers (4, 6, 8, 10). Concerning the sensitivity to the parameter, it is important to note that, in our newly proposed GMCA-HU method, we apply a threshold descent strategy during the iteration, so only one parameter needs to be tuned beforehand, which is related with the final threshold computation $\sigma$. This parameter $\sigma$ will be multiplied by the estimated noise standard deviation, and then used as a threshold value for the next iteration. When the SNR is low, $\sigma$ is generally set to a value smaller than 1, so as to suppress the noise disturbance in the decomposed results, while for higher SNR values, $\sigma$ is usually within the range of [1, 10] (the higher the SNRs, the larger the $\sigma$). So in the last synthetic experiment, we choose a synthetic HSI scene simulated with six endmembers and the threshold corresponding abundance fractions with 0.8. Then, a series of different values of $\sigma$ was analyzed experimentally.

Furthermore, the other parameters that are required for the GMCA-HU method were fixed in advance in all experiments. Concretely, for the outer layer optimization iteration, the maximum number of iterations is set to 500, while for the two inner layer optimization iterations, the maximum number

TABLE I

AVERAGE SAD BETWEEN THE OBTAINED AND REFERENCE (GROUND-TRUTH) ENDMEMBER SIGNATURES FOR THE GMCA-HU METHOD (SIMULATED DATA EXPERIMENTS)

| | Number of Endmembers | | | | | | | |
|---|---|---|---|---|---|---|---|---|
| | 4 | | 6 | | 8 | | 10 | |
| SNR | low | high | low | high | low | high | low | high |
| 10 | 0.0505 | 0.0655 | 0.0974 | 0.0983 | 0.124 | 0.151 | 0.1577 | 0.1852 |
| 30 | 0.0421 | 0.0632 | 0.0665 | 0.0871 | 0.0818 | 0.0889 | 0.0817 | 0.1345 |
| 50 | 0.0464 | 0.1093 | 0.0799 | 0.0525 | 0.0535 | 0.0594 | 0.0356 | 0.0527 |
| 70 | 0.0462 | 0.0881 | 0.0667 | 0.0536 | 0.0633 | 0.0527 | 0.0224 | 0.0465 |
| Inf | 0.0357 | 0.0959 | 0.0758 | 0.0828 | 0.0681 | 0.0623 | 0.0143 | 0.0439 |

TABLE II

RMSE BETWEEN THE ESTIMATED AND REFERENCE (GROUND-TRUTH) ABUNDANCES FOR THE GMCA-HU METHOD (SIMULATED DATA EXPERIMENTS)

| | Number of Endmembers | | | | | | | |
|---|---|---|---|---|---|---|---|---|
| | 4 | | 6 | | 8 | | 10 | |
| SNR | low | high | low | high | low | high | low | high |
| 10 | 0.245 | 0.1888 | 0.2022 | 0.1883 | 0.1977 | 0.2063 | 0.1992 | 0.183 |
| 30 | 0.2271 | 0.2193 | 0.2187 | 0.1926 | 0.169 | 0.1691 | 0.1906 | 0.1696 |
| 50 | 0.2176 | 0.2201 | 0.2401 | 0.1179 | 0.1993 | 0.1634 | 0.1613 | 0.1628 |
| 70 | 0.2136 | 0.1685 | 0.2387 | 0.2178 | 0.1959 | 0.1643 | 0.1911 | 0.1553 |
| Inf | 0.1614 | 0.1942 | 0.1703 | 0.2036 | 0.1664 | 0.1567 | 0.1898 | 0.1396 |

of iterations are both set to 80. When starting the optimization process, $\mathbf{M}$ is initialized with the first $p$ principal components ($p$ being the number of endmembers), and $\mathbf{S}$ is initialized as $\mathbf{M}^T\mathbf{Y}$. Then, the alternation between ANLS updates and constrained FBS updates is executed a few times, thus completing the initialization process. It should be noted that, in the initialization process, the regularization parameter $\lambda$ is set to 0 for the FBS updates. That is, before entering the main iteration looping, it is hoped that both the obtained $\mathbf{M}$ and $\mathbf{S}$ satisfy the nonnegative constraint, and with smaller residual and noise interference, thus accelerating the iterative convergence of the algorithm. After that, in the main loop, the initial value of $\lambda$ is set to $\|\mathbf{M}^T(\mathbf{MS}-\mathbf{Y})\|_\infty$, which forces the coefficients of $\mathbf{S}$ to be nonincreasing in the first iteration, and then gradually descend to the $\sigma \times res\_std$, where $res\_std$ is the estimation of noise standard deviation on the current residual, which can refine the solution while preserving continuity.

For the other compared unmixing methods, the corresponding parameters have been set follows. Concerning the MVC-NMF, the VCA + FCLS is first executed to generate an initial endmember set and abundances. Then, 80 iterations (with a tolerance value of $1e$-6) are used to achieve a relatively robust stopping condition, and the corresponding annealing temperature is set to 0.015. For the R-CoNMF unmixing method, parameter settings have been optimized as detailed in [27].

Finally, we would like to emphasize that all the experiments were conducted using MATLAB R2015a in a desktop PC equipped with an Intel Core i7 CPU (at 3.6 GHz) and 32 GB of RAM.

### C. Analysis of the Experimental Results

*1) Noise Robustness:* In this experiment, we conduct a comparative analysis on robustness to noise of the proposed unmixing method. As described above, five different SNR levels are considered, varying from 10 dB to $+\infty$ (no noise added) with a step size of 20 dB. Tables I and II show the results of the SAD and RMSE metrics obtained by the proposed GMCA-HU method under different SNRs, as well as different numbers of endmembers and degrees of mixture in the simulated pixels. As can be observed from Tables I and II, although the SAD value is smaller when the SNR becomes larger, the difference is not obvious, especially when the number of endmembers and the degree of mixture are low. As the number of endmembers increase, the results for SNRs below 30 dB are similar to those for SNRs above 30 dB. As a result, it can be concluded that the proposed GMCA-HU exhibits robustness with respect to different SNRs.

In order to outline the superiority of the proposed GMCA-HU method, Fig. 3 provides a comparison between the average SAD of four different unmixing methods under different SNRs, different number of endmembers, and different mixture degrees of the simulated pixels. In Fig. 3, the first row illustrates the SAD results under a low mixture degree scheme (with $\theta = 0.8$), while the second row illustrates the SAD results under a higher mixture degree scheme (with $\theta = 0.6$). As can be observed, all the considered four unmixing methods exhibit a decrease in the SAD results when the SNR decreases. When the SNR is high, the R-CoNMF generally achieves the best unmixing result for a low degree of mixture in the simulated pixels. However, when the SNR becomes lower, the noise corruption introduced in the MVC-NMF and R-CoNMF algorithms is much higher than that introduced in our GMCA-HU method. On the contrary, the GMCA-HU exhibits much better robustness to noise. This is due to the fact that both the MVC-NMF and R-CoNMF impose a simplex volume constraint, which is very sensitive to noise.

*2) Mixture Degree of Simulated Pixels:* The purpose of this experiment is to analyze the performance of the GMCA-HU method under different mixture degrees of simulated pixels. Generally, the lower the mixture degree, the better the SAD results. As we can observe from the first row of Fig. 3, GMCA-HU method is not the best one for a low mixture degree (R-CoNMF obtains the best SAD scores in most cases).

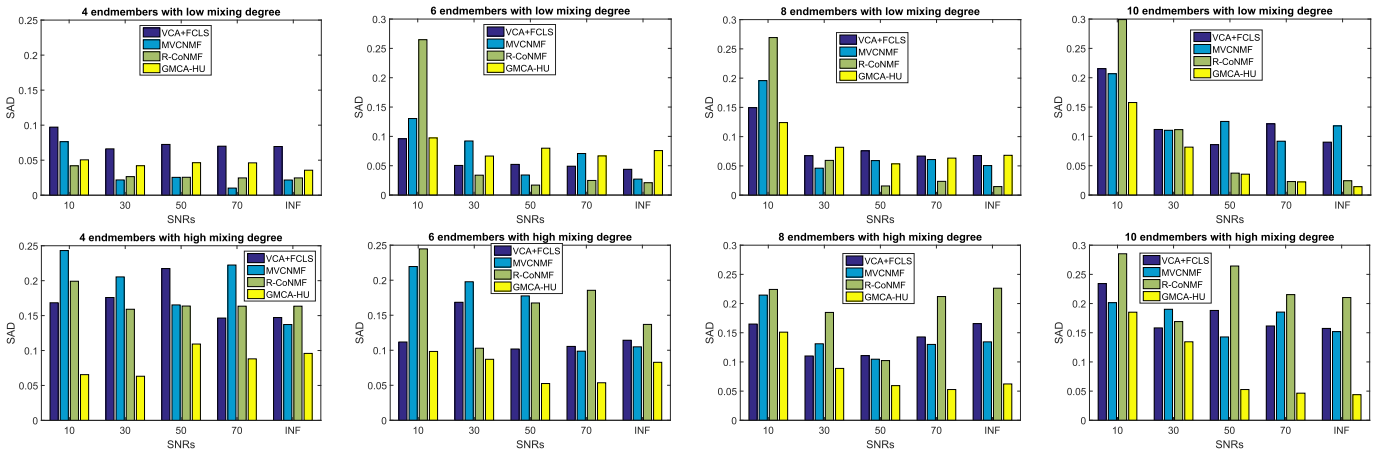


Fig. 3. Comparison of the average SAD of different unmixing methods under a high mixture degree of simulated pixels ($\theta = 0.6$) and a low mixture degree of simulated pixels ($\theta = 0.8$), respectively.

However, as shown in the second row of Fig. 3, the SAD results of GMCA-HU are the best under a high mixture degree of pixels. Moreover, we can observe from Table I that GMCA-HU is nonsensitive to the mixture degree, especially in the case of low SNRs. Overall, the experimental results reveal that GMCA-HU method has an obvious insensitivity with respect to the mixture degree, which is a highly desirable feature. Considering that very highly mixed pixels are present in many real HSI scenes, such merit is expected to bring significant application value to our newly developed method.

Furthermore, we illustrate the obtained abundance maps, as well as the RMSE results calculated by using (19), of the four compared methods under different mixture degrees, in which the results are obtained from a synthetic HSI scene simulated with four endmembers and SNR of 10 dB, as shown in Figs. 4 and 5, respectively. Fig. 4 shows the estimated abundance maps under a low mixture degree scheme (with $\theta = 0.8$), where the first column displays the ground-truth abundances (without noise contamination) and the other columns display the abundances estimated by different unmixing methods. It can be observed that the abundances of R-CoNMF method are closer to the ground-truth abundances than the other three methods. For our proposed GMCA-HU method, though the result of RMSE is weaker than the R-CoNMF method, and not much better than the MVCNMF method, it can maintain spatial consistency and morphological characteristics as R-CoNMF method. While for the VCA + FCLS method, it suffers from certain ambiguities in terms of spatial distribution and morphology, especially for the first and third abundance maps, which all show a very ambiguous spatial distribution. Moreover, in the case of a high mixture degree scheme (with $\theta = 0.6$, shown in Fig. 5), the spatial distribution and morphology are better maintained by the GMCA-HU method, while for the R-CoNMF and MVCNMF methods, certain degree of over-smoothing still exist in the obtained abundance maps.

*3) Number of Endmembers:* Finally, we conducted an experiment to investigate the sensitivity of the GMCA-HU method to the presence of different numbers of endmembers in the simulated data. In general, the higher the number of endmembers, the more difficult the unmixing process is. However, it can be observed from Fig. 3 that the SAD results of the GMCA-HU method are stable for different numbers of endmembers. For example, when the simulated scene was constructed using eight and ten endmembers, our GMCA-HU still provided very good SAD results. A similar situation can be observed from the SAD results of the R-CoNMF method (for example, when eight endmembers were simulated in the scene, R-CoNMF was better than GMCA-HU while, when ten endmembers were simulated, our GMCA-HU provided better results). In addition, under a high mixture degree scheme, GMCA-HU obtained the best SAD scores (especially for a large number of endmembers). As a result, we can conclude that the proposed GMCA-HU method is more stable than other unmixing methods when the number of endmembers increases.

*4) Analysis on the Parameter $\sigma$:* In this experiment, we report the plots of average SAD based on different parameter $\sigma$ by using generated synthetic scene. The adopted synthetic image has six number of endmembers, and under low degree of mixture (with threshold of abundance fractions is 0.8). Four different SNRs, including 10, 30, 50, and 70 dB, are considered in this experiment. For the SNRs of 10 and 30 dB, the parameter $\sigma$ is set from 0.5 to 5 with a step size of 0.5. While for the SNRs of 50 and 70 dB, the parameter $\sigma$ is set from 1 to 10 with a step size of 1. Beyond that, the other parameters that are required are all the same as Section III-B. The plots of average SAD by using different parameter $\sigma$ are given in Fig. 6.

It can be observed from Fig. 6 that, for the low SNRs circumstances, such as 10 and 30 dB, the smaller the $\sigma$, the better the average SAD result. When SNR is 10 dB, the best SAD result comes from $\sigma = 0.5$, while for the 30 dB, the best SAD result comes from $\sigma = 1$. However, different results are reflected in the high SNR circumstances, such as 50 and 70 dB, the average SAD results go through a process of decreasing and then slowly increasing. When SNR is 50 dB, the best SAD result comes from $\sigma = 3$, while for the 70 dB, the best SAD result comes from $\sigma = 4$. As a result, it is expected that when the SNR is low, $\sigma$ is suggested to set

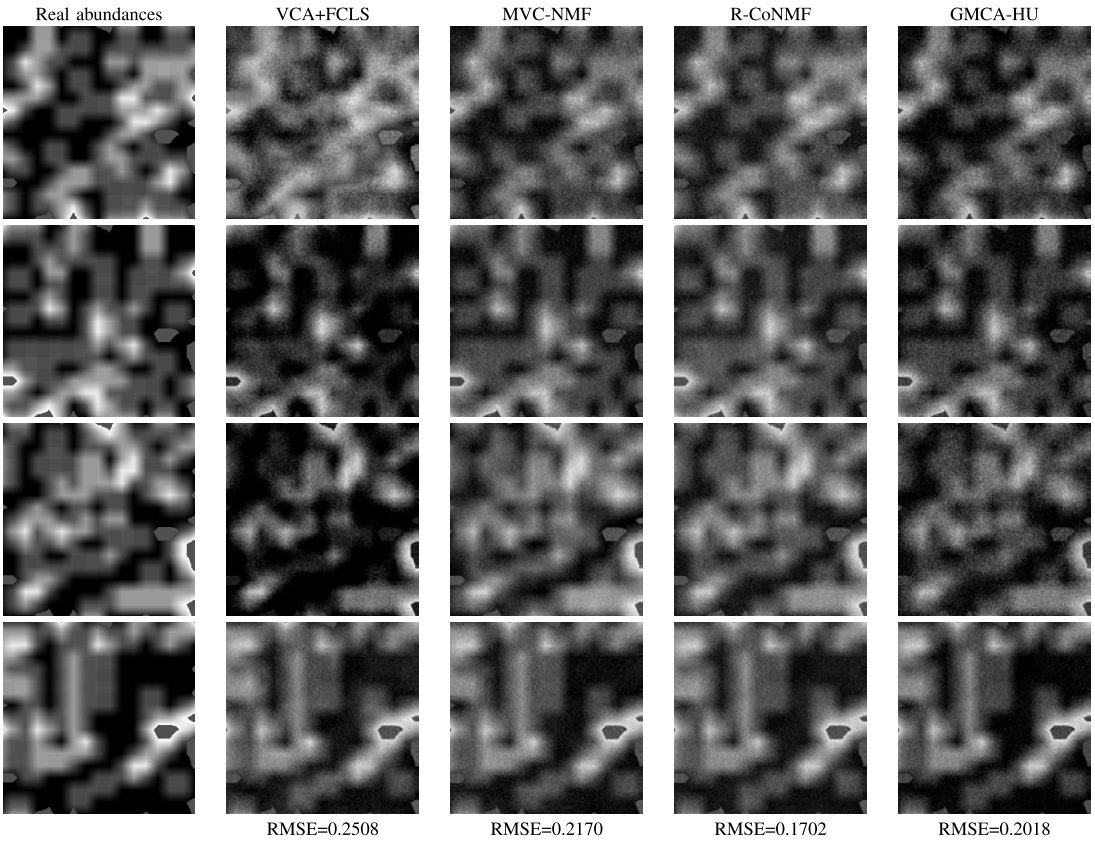


Fig. 4. Abundances estimated by different unmixing methods for a simulated scene with four endmembers, low mixture degree ($\theta = 0.8$), and low SNR (10 dB).

a value smaller than 1, so as to suppress the noise disturbance, while for higher SNR, $\sigma$ is suggested to set larger than 1, and the higher the SNRs, the larger the $\sigma$.

## IV. Experiments on Real Data

In this section, two benchmark HSI data sets are chosen for assessing the performance of the proposed GMCA-HU method: an urban scene acquired by the hyperspectral digital image collection experiment (HYDICE), and the Cuprite scene acquired by the Airborne Visible Infra-Red Imaging Spectrometer (AVIRIS).

### *A. Experiments on the HYDICE Urban Scene*

The Urban scene has a size of $307 \times 307$ pixels and 210 spectral bands and was acquired by the HYDICE at Copperas Cove, TX, US, in October 1995. This scene has a spatial resolution of $2 \times 2$ m$^2$ and spectral resolution of 10 nm (covering the wavelength range from 0.4 to 2.5 $\mu$m). After removing those spectral bands with dense water vapor, we retain a total of 162 bands in our experiments. Fig. 7(a) shows a false color composition of the image, and Fig. 7(b) shows four endmember classes: asphalt, roof, grass, and tree that are used as representative ground classes in the scene. As can be seen in Fig. 7, the signatures of grass and trees exhibit very similar spectral shape, which makes their separation difficult.

Table III presents the SAD results obtained by the four compared unmixing methods for the Urban scene, including the SAD results of each ground class and an average value. For our proposed GMCA-HU method, the threshold computation parameter of $\sigma$ is set to 10, and the other parameters that are required are the same as mentioned in Section III-B. As can be observed, our GMCA-HU method obtained a very good unmixing result in terms of SAD, especially for the grass and tree classes, whereas the other methods found certain difficulties with these two ground classes. In fact, our method benefits from the spatial morphological diversity that is presented in the scene, which can help separate spectrally similar ground classes (such as grass and trees) due to their diverse spatial distribution and structural details. In addition, Fig. 8 shows the obtained endmember signatures and the corresponding abundance maps, in which the grayscale values (from black to white) represent abundance values (from 0 to 1). For comparison purposes, we also give the reference abundance maps (shown in the first row of Fig. 8). In Fig. 8,

TABLE III
SAD Between the Reference and the Obtained Endmembers (Using Different Methods) From the Urban HYDICE Scene

| | VCA+FCLS | MVC-NMF | R-CoNMF | GMCA-HU |
|---|---|---|---|---|
| Asphalt | 0.2117 | 0.2026 | 0.126 | 0.0966 |
| Roof | 0.656 | 0.4717 | 0.0517 | 0.0317 |
| Grass | 0.3616 | 0.3762 | 0.223 | 0.0339 |
| Tree | 0.1125 | 0.2641 | 0.1287 | 0.0347 |
| Avg | 0.3355 | 0.3287 | 0.1324 | 0.0492 |

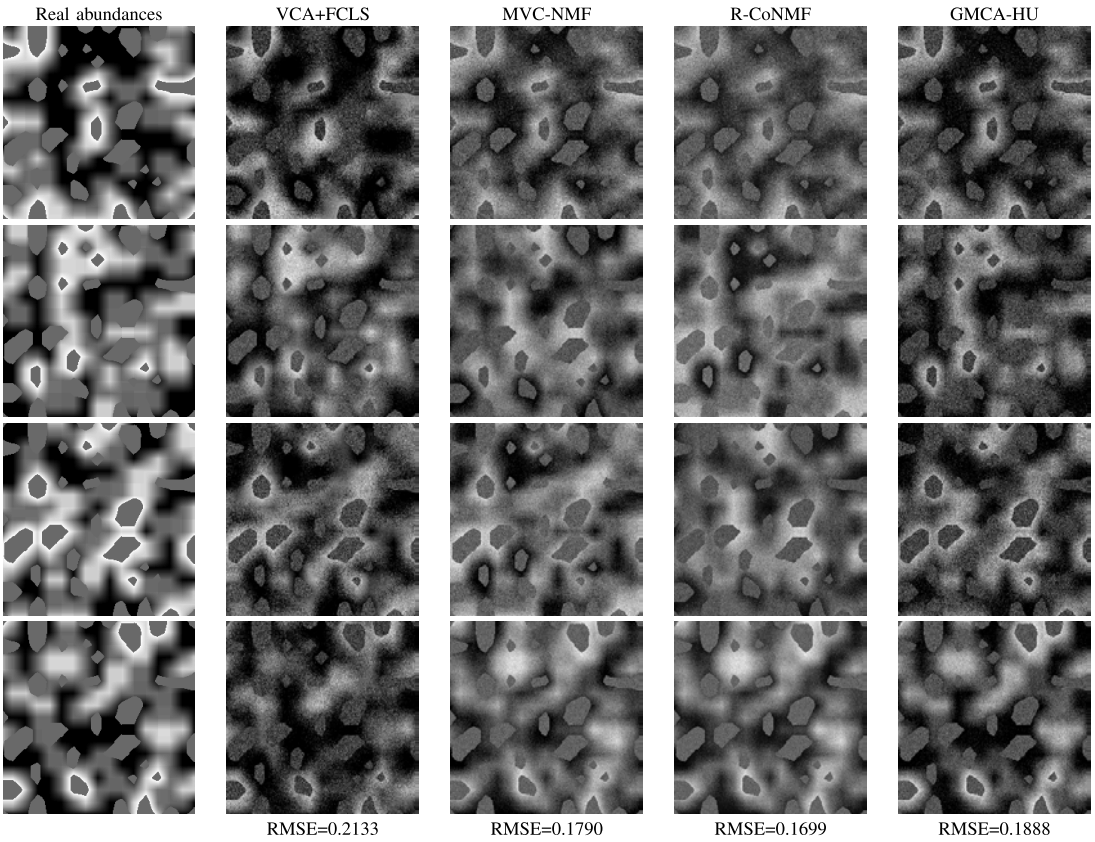


Fig. 5. Abundances estimated by different unmixing methods for a simulated scene with four endmembers, high mixture degree ($\theta = 0.6$), and low SNR (10 dB).

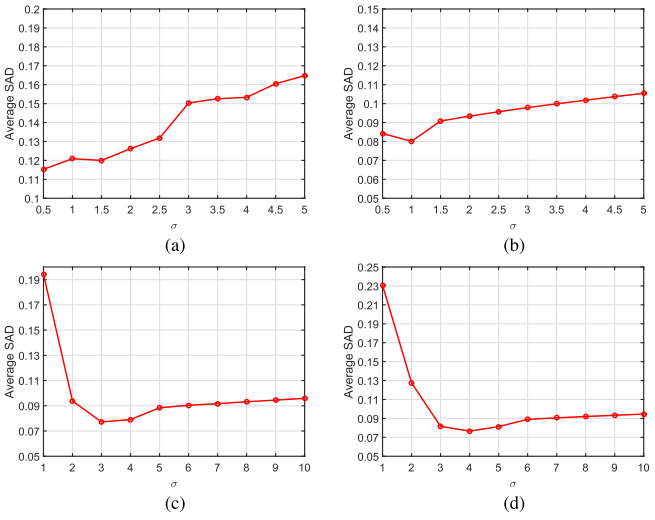


Fig. 6. Plots of average SAD obtained by different parameter $\sigma$ under different SNRs of the synthetic data sets. (a) SNR = 10 dB. (b) SNR = 30 dB. (c) SNR = 50 dB. (d) SNR = 70 dB.

we can observe the very clear spatial distribution of the four considered ground classes. The asphalt class, for instance, displays a very distinctive linear structure. For the grass class, a regional block structure can also be observed. For the roof and tree classes, smaller patch-structures are scattered in the scene. Overall, these abundance maps accurately represent the spatial distribution of different classes in the scene. Moreover, Fig. 8 presents a comparison of the obtained versus the

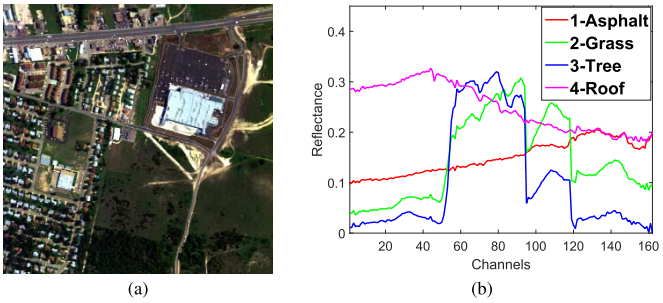


Fig. 7. (a) Urban HYDICE scene. (b) Endmember signatures considered in experiments.

reference spectral signatures. It can be observed that the spectral signatures match very well the reference grass and tree classes. For the asphalt and roof, there still exist certain spectral disturbances. Overall, the experimental results obtained with the Urban HYDICE scene indicated the advantages of using spatial morphological characteristics for unmixing purposes.

### *B. Experiments on the AVIRIS Cuprite Scene*

The second real HSI scene is the well-known Cuprite data set, which was collected by the AVIRIS sensor on June 19, 1997. The portion that is used in our experiments has 250 $\times$ 191 pixels and 224 spectral bands covering a wavelength range from 0.4 to 2.5 $\mu$m, with a spectral resolution of 10 nm and spatial resolution of 20 m/pixel. After removing bands of 1 and 2, 105–115, 150–170, and 223 and

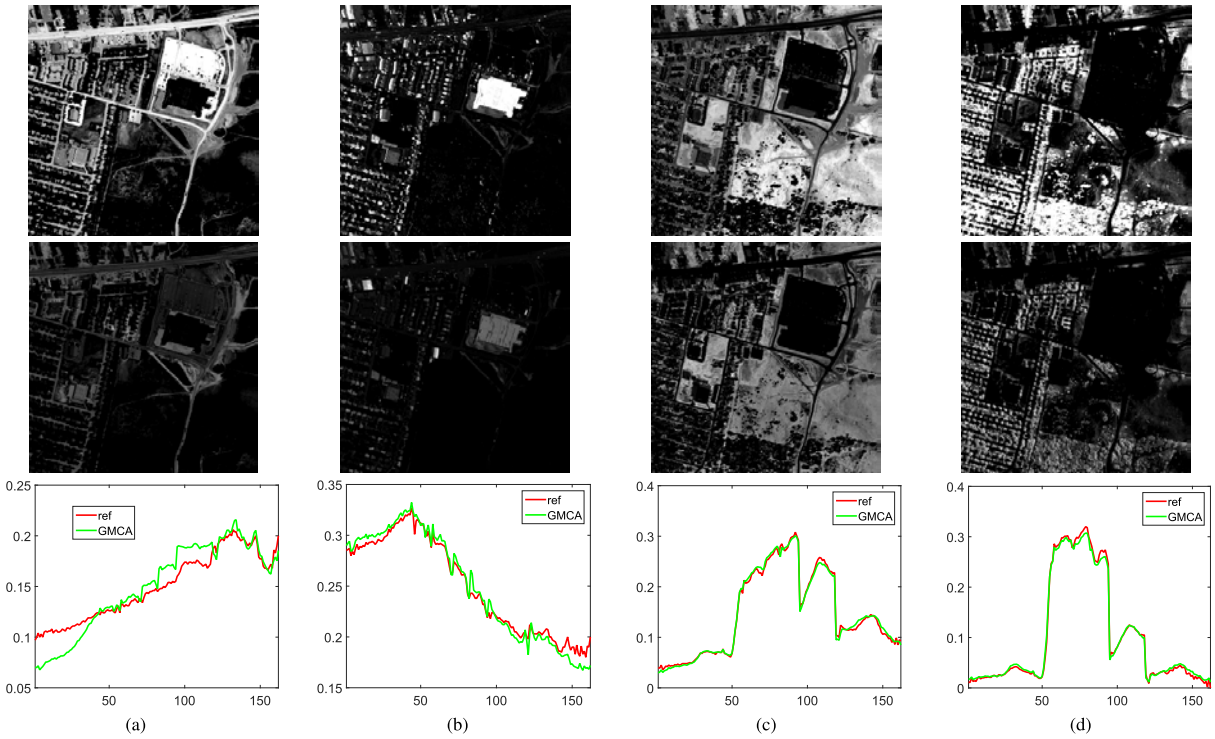


Fig. 8. Abundance maps and endmember signatures obtained for the Urban HYDICE scene by the proposed GMCA-HU method (for clarity, each obtained signature is displayed together with its reference counterpart). (a) Asphalt. (b) Roof. (c) Grass. (d) Tree.

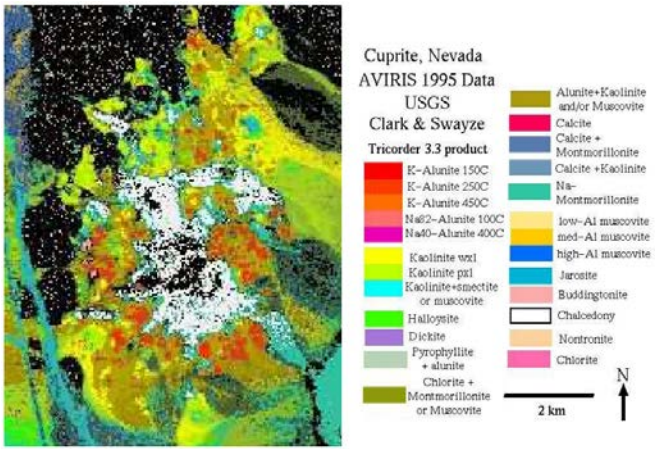


Fig. 9. Mineral distribution map in the Cuprite mining district.

TABLE IV

SAD BETWEEN THE REFERENCE AND THE OBTAINED ENDMEMBERS (USING DIFFERENT METHODS) FROM THE AVIRIS CUPRITE SCENE

| | VCA+FCLS | MVC-NMF | R-CoNMF | GMCA-HU |
|---|---|---|---|---|
| Alunite | 0.0779 | 0.1753 | 0.0613 | 0.0808 |
| Andradite | 0.0597 | 0.0669 | 0.1549 | 0.0886 |
| Buddingtonite | 0.1134 | 0.0895 | 0.1224 | 0.1481 |
| Chalcedony | 0.1599 | 0.1626 | 0.0921 | 0.1343 |
| Dumortierite | 0.1495 | 0.27 | 0.1622 | 0.1154 |
| Jarosite | 0.0936 | 0.1306 | 0.1617 | 0.1228 |
| Kaolinite | 0.188 | 0.1526 | 0.2003 | 0.1132 |
| Kaolin-1 | 0.0732 | 0.0896 | 0.197 | 0.0603 |
| Kaolin-2 | 0.0629 | 0.0632 | 0.1048 | 0.1515 |
| Montmorillonite | 0.083 | 0.0653 | 0.1031 | 0.1047 |
| Muscovite | 0.0811 | 0.1493 | 0.0703 | 0.0703 |
| Nontronite | 0.1189 | 0.1244 | 0.0962 | 0.1094 |
| Avg | 0.1051 | 0.1283 | 0.1272 | 0.1083 |

224 due to water absorption and low SNR, we retain a total of 188 reflectance channels to be used in the experiments. The Cuprite site is well understood mineralogically and has several exposed minerals of interest, all included in the USGS library (used in this article to obtain reference counterparts for each extracted endmember). Fig. 9 shows a mineral distribution map in this Cuprite mining district, which is available online.[1] In the following experiments, we will select a few highly representative mineral spectra from the USGS library to examine the purity of the endmembers extracted by different unmixing methods from the Cuprite mining district.

[1]http://speclab.cr.usgs.gov/cuprite95.tgif.2.2um_map.gif

It should be mentioned that the number of endmembers in this scene is very hard to determine due to the complex composition of minerals. With this consideration in mind, we adopted an assumption of 12 endmembers for the considered subscene, as it is commonly suggested in the public literatures. For the adopted GMCA-HU method, the threshold computation parameter of $\sigma$ is set to 12, and the other parameters that are required are the same as Section III-B. Table IV presents the SAD results for each ground class as well as an average value. The corresponding estimated endmember signatures and abundance maps are also presented in Figs. 10 and 11.

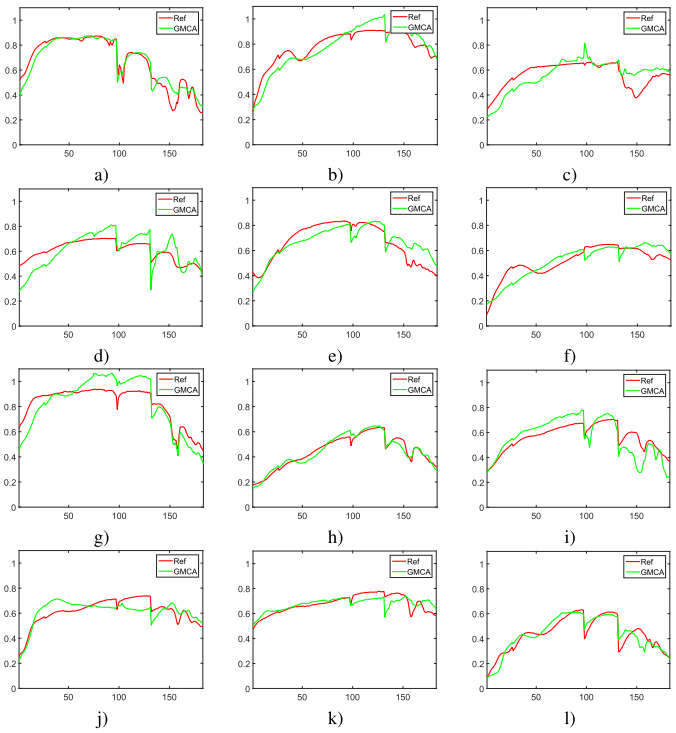


Fig. 10. Endmember signatures extracted from the AVIRIS Cuprite scene by the proposed GMCA-HU method (for clarity, each obtained signature is displayed together with its USGS library signature counterpart). (a) Alunite. (b) Andradite. (c) Buddingtonite. (d) Chalcedony. (e) Dumortierite. (f) Jarosite. (g) Kaolinite. (h) Kaolin-1. (i) Kaolin-2. (j) Montmorillonite. (k) Muscovite. (l) Nontronite.

It can be observed from Table IV that, for the Muscovite and Nontronite minerals, GMCA-HU and R-CoNMF obtained lower SAD scores than the MVC-NMF and VCA + FCLS methods, while for the Dumortierite, Kaolinite and Kaolin-1 minerals, GMCA-HU obtained better SAD scores than the other three methods. Considering the average SAD results, GMCA-HU obtained a very promising result. However, the advantages of GMCA-HU in this particular case are not so obvious. The main reason is that the abundance maps of some mineral classes tend to be fragmented and with little spatial consistency, thus weakening the impact of including spatial morphological diversity in the unmixing process.

In Fig. 10, the spectral signatures of the endmembers extracted by our method and their corresponding USGS library signature counterparts are shown. In this case, the match between each endmember and its corresponding USGS library signature has been built by using both visual interpretation and the SAD score between the obtained spectral signature and its corresponding library signature. It should be emphasized that, due to the complexity and variability of some of the mineral classes, we compared the estimated endmember signatures with the USGS library signatures (acquired in perfect conditions). With this consideration in mind, the results from Fig. 10 indicate that the endmembers estimated by our method provide a good match with regard to the corresponding library signatures.

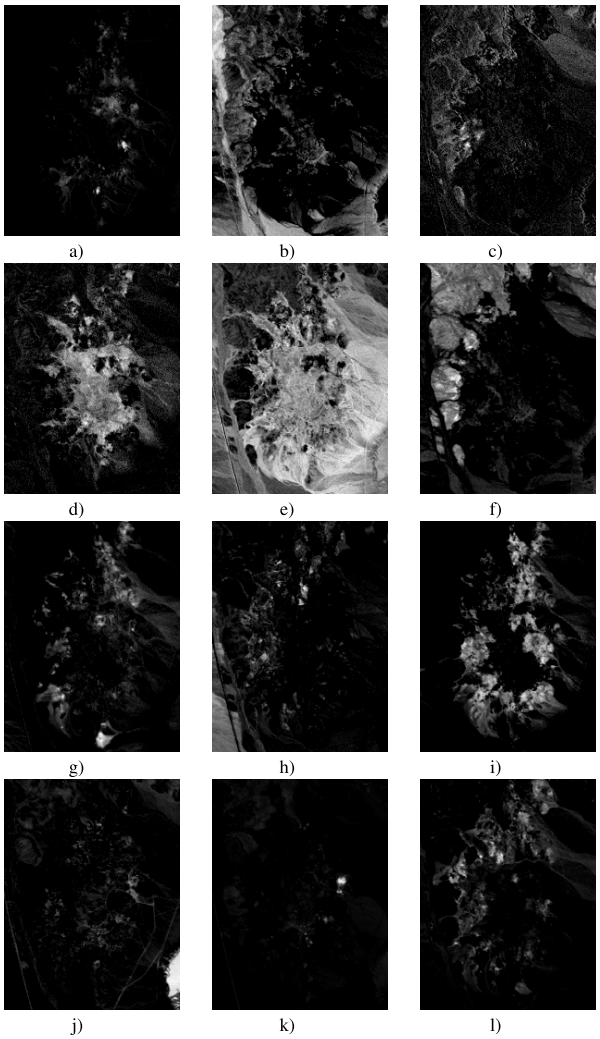


Fig. 11. Abundance maps obtained for the Cuprite mineral scene by the proposed GMCA-HU method. (a) Alunite. (b) Andradite. (c) Buddingtonite. (d) Chalcedony. (e) Dumortierite. (f) Jarosite. (g) Kaolinite. (h) Kaolin-1. (i) Kaolin-2. (j) Montmorillonite. (k) Muscovite. (l) Nontronite.

## V. Conclusion and Future Research

In this article, a new blind unmixing method has been developed for HSI. Our newly developed method is based on GMCA, which naturally includes spatial information in the unmixing process by accounting for the sparsity and morphological diversity of the abundance maps associated with each endmember. Furthermore, in order to obtain a stable optimization solution, an alternative iteration constrained algorithm with a threshold descent strategy has been adopted. The obtained experimental results reveal that the proposed blind unmixing strategy can lead to stable and very accurate results, able to include the spatial characteristics of the scene when conducting the unmixing process, as well as fast processing speed. As with any new approach, there are some unresolved issues that deserve further consideration in the future developments. First, although there is just one single parameter ($\sigma$) that needs to be tuned in our GMCA-HU method, it is still hard to determine (considering that $\sigma$ is related with the noise standard deviation of the residual, how to estimate the noise standard deviation more accurately deserves

further investigation). Second, as shown in (9), the sparsity and diversity of the coefficients can promote source separation. However, considering the difficulty of the optimization solution corresponding to the transform domain, in our proposed model we transfer the sparsity of coefficients into the sparsity of the sources for simplicity. At this point, we emphasize that sparse representation in the transformed coefficient domain is more efficient than that in the source domain. Therefore, there is a need to perform GMCA on the transformed domain in the future developments.

## ACKNOWLEDGMENT

The authors would like to thank the Editors and the Anonymous Reviewers for their detailed comments and suggestions, which greatly helped us to improve the clarity and presentation of our manuscript.

## REFERENCES

[1] J. M. Bioucas-Dias, A. Plaza, G. Camps-Valls, P. Scheunders, N. M. Nasrabadi, and J. Chanussot, "Hyperspectral remote sensing data analysis and future challenges," *IEEE Geosci. Remote Sens. Mag.*, vol. 1, no. 2, pp. 6–36, Jun. 2013.

[2] L. Zhang and B. Du, "Recent advances in hyperspectral image processing," *Geo-Spatial Inf. Sci.*, vol. 15, no. 3, pp. 143–156, 2012.

[3] X. Lu, B. Wang, X. Zheng, and X. Li, "Exploring models and data for remote sensing image caption generation," *IEEE Trans. Geosci. Remote Sens.*, vol. 56, no. 4, pp. 2183–2195, Apr. 2018.

[4] X. Lu, W. Zhang, and X. Li, "A coarse-to-fine semi-supervised change detection for multispectral images," *IEEE Trans. Geosci. Remote Sens.*, vol. 56, no. 6, pp. 3587–3599, Jun. 2018.

[5] J. M. Bioucas-Dias *et al.*, "Hyperspectral unmixing overview: Geometrical, statistical, and sparse regression-based approaches," *IEEE J. Sel. Topics Appl. Earth Observ. Remote Sens.*, vol. 5, no. 2, pp. 354–379, Apr. 2012.

[6] A. Plaza, G. Martín, J. Plaza, M. Zortea, and S. Sánchez, "Recent developments in endmember extraction and spectral unmixing," in *Optical Remote Sensing*. Berlin, Germany: Springer, 2011, pp. 235–267.

[7] M. Tang, L. Gao, A. Marinoni, P. Gamba, and B. Zhang, "Integrating spatial information in the normalized p-linear algorithm for nonlinear hyperspectral unmixing," *IEEE J. Sel. Topics Appl. Earth Observ. Remote Sens.*, vol. 11, no. 4, pp. 1179–1190, Apr. 2018.

[8] M. Tang, B. Zhang, A. Marinoni, L. Gao, and P. Gamba, "Multiharmonic postnonlinear mixing model for hyperspectral nonlinear unmixing," *IEEE Geosci. Remote Sens. Lett.*, vol. 15, no. 11, pp. 1765–1769, Nov. 2018.

[9] J. C. Harsanyi and C.-I. Chang, "Hyperspectral image classification and dimensionality reduction: An orthogonal subspace projection approach," *IEEE Trans. Geosci. Remote Sens.*, vol. 32, no. 4, pp. 779–785, Jul. 1994.

[10] J. W. Boardman, F. A. Kruse, and R. O. Green, "Mapping target signatures via partial unmixing of AVIRIS data," in *Proc. 5th JPL Airborne Earth Sci. Workshop*, Pasadena, CA, USA: Jet Propuls. Lab., 1995, pp. 23–26.

[11] M. E. Winter, "N-FINDR: An algorithm for fast autonomous spectral end-member determination in hyperspectral data," *Proc. SPIE*, vol. 3753, pp. 266–275, Oct. 1999.

[12] J. M. P. Nascimento and J. M. Bioucas-Dias, "Vertex component analysis: A fast algorithm to unmix hyperspectral data," *IEEE Trans. Geosci. Remote Sens.*, vol. 43, no. 4, pp. 898–910, Apr. 2005.

[13] J. M. Bioucas-Dias, "A variable splitting augmented Lagrangian approach to linear spectral unmixing," in *Proc. 1st Workshop Hyperspectral Image Signal Process., Evol. Remote Sens.*, Aug. 2009, pp. 1–4.

[14] J. Li, A. Agathos, D. Zaharie, J. M. Bioucas-Dias, A. Plaza, and X. Li, "Minimum volume simplex analysis: A fast algorithm for linear hyperspectral unmixing," *IEEE Trans. Geosci. Remote Sens.*, vol. 53, no. 9, pp. 5067–5082, Sep. 2015.

[15] M.-D. Iordache, J. Bioucas-Dias, and A. Plaza, "Sparse unmixing of hyperspectral data," *IEEE Trans. Geosci. Remote Sens.*, vol. 49, no. 6, pp. 2014–2039, Jun. 2011.

[16] B. Somers, G. P. Asner, L. Tits, and P. Coppin, "Endmember variability in spectral mixture analysis: A review," *Remote Sens. Environ.*, vol. 115, no. 7, pp. 1603–1616, 2011.

[17] L. Gao, L. Zhuang, and B. Zhang, "Region-based estimate of endmember variances for hyperspectral image unmixing," *IEEE Geosci. Remote Sens. Lett.*, vol. 13, no. 12, pp. 1807–1811, Dec. 2016.

[18] J. Franke, D. A. Roberts, K. Halligan, and G. Menz, "Hierarchical multiple endmember spectral mixture analysis (MESMA) of hyperspectral imagery for urban environments," *Remote Sens. Environ.*, vol. 113, no. 8, pp. 1712–1723, 2009.

[19] D. Heslop, T. V. Dobeneck, and M. Höcker, "Using non-negative matrix factorization in the 'unmixing' of diffuse reflectance spectra," *Marine Geol.*, vol. 241, nos. 1–4, pp. 63–78, 2007.

[20] T. Zhi, B. Yang, Z. Chen, and B. Wang, "Nonnegative matrix factorization with constraints on endmember and abundance for hyperspectral unmixing," in *Proc. IEEE Int. Geosci. Remote Sens. Symp. (IGARSS)*, Jul. 2017, pp. 1149–1152.

[21] L. Miao and H. Qi, "Endmember extraction from highly mixed data using minimum volume constrained nonnegative matrix factorization," *IEEE Trans. Geosci. Remote Sens.*, vol. 45, no. 3, pp. 765–777, Mar. 2007.

[22] Y. Yu and W. Sun, "Minimum distance constrained non-negative matrix factorization for the endmember extraction of hyperspectral images," *Proc. SPIE*, vol. 6790, Nov. 2007, Art. no. 679015.

[23] V. P. Pauca, J. Piper, and R. J. Plemmons, "Nonnegative matrix factorization for spectral data analysis," *Linear Algebra Appl.*, vol. 416, no. 1, pp. 29–47, 2006.

[24] S. Jia and Y. Qian, "Constrained nonnegative matrix factorization for hyperspectral unmixing," *IEEE Trans. Geosci. Remote Sens.*, vol. 47, no. 1, pp. 161–173, Jan. 2009.

[25] Y. Qian, S. Jia, J. Zhou, and A. Robles-Kelly, "Hyperspectral unmixing via $L_{1/2}$ sparsity-constrained nonnegative matrix factorization," *IEEE Trans. Geosci. Remote Sens.*, vol. 49, no. 11, pp. 4282–4297, Nov. 2011.

[26] Z. Yang, G. Zhou, S. Xie, S. Ding, J.-M. Yang, and J. Zhang, "Blind spectral unmixing based on sparse nonnegative matrix factorization," *IEEE Trans. Image Process.*, vol. 20, no. 4, pp. 1112–1125, Apr. 2011.

[27] J. Li, J. M. Bioucas-Dias, A. Plaza, and L. Liu, "Robust collaborative nonnegative matrix factorization for hyperspectral unmixing," *IEEE Trans. Geosci. Remote Sens.*, vol. 54, no. 10, pp. 6076–6090, Oct. 2016.

[28] W. He, H. Zhang, and L. Zhang, "Total variation regularized reweighted sparse nonnegative matrix factorization for hyperspectral unmixing," *IEEE Trans. Geosci. Remote Sens.*, vol. 55, no. 7, pp. 3909–3921, Jul. 2017.

[29] X. Lu, W. Zhang, and X. Li, "A hybrid sparsity and distance-based discrimination detector for hyperspectral images," *IEEE Trans. Geosci. Remote Sens.*, vol. 56, no. 3, pp. 1704–1717, Dec. 2018.

[30] P. V. Giampouras, A. A. Rontogiannis, and K. D. Koutroumbas, "Low-rank and sparse NMF for joint endmembers' number estimation and blind unmixing of hyperspectral images," in *Proc. 25th Eur. Signal Process. Conf. (EUSIPCO)*, Aug./Sep. 2017, pp. 1430–1434.

[31] C. G. Tsinos, A. A. Rontogiannis, and K. Berberidis, "Distributed blind hyperspectral unmixing via joint sparsity and low-rank constrained non-negative matrix factorization," *IEEE Trans. Comput. Imag.*, vol. 3, no. 2, pp. 160–174, Jun. 2017.

[32] M. Wang, B. Zhang, X. Pan, and S. Yang, "Group low-rank nonnegative matrix factorization with semantic regularizer for hyperspectral unmixing," *IEEE J. Sel. Topics Appl. Earth Observ. Remote Sens.*, vol. 11, no. 4, pp. 1022–1029, Apr. 2018.

[33] X. Zhang, J. Zhang, C. Li, C. Cheng, L. Jiao, and H. Zhou, "Hybrid unmixing based on adaptive region segmentation for hyperspectral imagery," *IEEE Trans. Geosci. Remote Sens.*, vol. 56, no. 7, pp. 3861–3875, Jul. 2018.

[34] Z. Xu, X. Chang, F. Xu, and H. Zhang, "$L_{1/2}$ regularization: A thresholding representation theory and a fast solver," *IEEE Trans. Neural Netw. Learn. Syst.*, vol. 23, no. 7, pp. 1013–1027, Jul. 2012.

[35] Y. E. Salehani and S. Gazor, "Smooth and sparse regularization for NMF hyperspectral unmixing," *IEEE J. Sel. Topics Appl. Earth Observ. Remote Sens.*, vol. 10, no. 8, pp. 3677–3692, Aug. 2017.

[36] X. Wang, Y. Zhong, L. Zhang, and Y. Xu, "Spatial group sparsity regularized nonnegative matrix factorization for hyperspectral unmixing," *IEEE Trans. Geosci. Remote Sens.*, vol. 55, no. 11, pp. 6287–6304, Nov. 2017.

[37] X. Liu, W. Xia, B. Wang, and L. Zhang, "An approach based on constrained nonnegative matrix factorization to unmix hyperspectral data," *IEEE Trans. Geosci. Remote Sens.*, vol. 49, no. 2, pp. 757–772, Feb. 2011.

[38] R. Liu, B. Du, and L. Zhang, "Hyperspectral unmixing via double abundance characteristics constraints based NMF," *Remote Sens.*, vol. 8, no. 6, pp. 464–486, 2016.
[39] X. Lu, H. Wu, Y. Yuan, P. Yan, and X. Li, "Manifold regularized sparse NMF for hyperspectral unmixing," *IEEE Trans. Geosci. Remote Sens.*, vol. 51, no. 5, pp. 2815–2826, May 2013.
[40] L. Tong, J. Zhou, Y. Qian, and Y. Gao, "Multiple graph regularized NMF for hyperspectral unmixing," in *Proc. 7th Workshop Hyperspectral Image Signal Process., Evol. Remote Sens. (WHISPERS)*, Jun. 2015, pp. 1–4.
[41] S. Yang, X. Zhang, Y. Yao, S. Cheng, and L. Jiao, "Geometric nonnegative matrix factorization (GNMF) for hyperspectral unmixing," *IEEE J. Sel. Topics Appl. Earth Observ. Remote Sens.*, vol. 8, no. 6, pp. 2696–2703, Jun. 2015.
[42] W. Wang, Y. Qian, and Y. Y. Tang, "Hypergraph-regularized sparse NMF for hyperspectral unmixing," *IEEE J. Sel. Topics Appl. Earth Observ. Remote Sens.*, vol. 9, no. 2, pp. 681–694, Feb. 2016.
[43] X. Li, J. Zhou, L. Tong, X. Yu, J. Guo, and C. Zhao, "Structured discriminative nonnegative matrix factorization for hyperspectral unmixing," in *Proc. IEEE Int. Conf. Image Process. (ICIP)*, Sep. 2016, pp. 1848–1852.
[44] B. Qian, J. Zhou, L. Tong, X. Shen, and F. Liu, "Nonnegative matrix factorization with endmember sparse graph learning for hyperspectral unmixing," in *Proc. IEEE Int. Conf. Image Process. (ICIP)*, Sep. 2016, pp. 1843–1847.
[45] L. Tong, J. Zhou, X. Li, Y. Qian, and Y. Gao, "Region-based structure preserving nonnegative matrix factorization for hyperspectral unmixing," *IEEE J. Sel. Topics Appl. Earth Observ. Remote Sens.*, vol. 10, no. 4, pp. 1575–1588, Apr. 2017.
[46] X.-R. Feng, H.-C. Li, J. Li, Q. Du, A. Plaza, and W. J. Emery, "Hyperspectral unmixing using sparsity-constrained deep nonnegative matrix factorization with total variation," *IEEE Trans. Geosci. Remote Sens.*, vol. 56, no. 10, pp. 6245–6257, Oct. 2018.
[47] X. Lu, Y. Chen, and X. Li, "Hierarchical recurrent neural hashing for image retrieval with hierarchical convolutional features," *IEEE Trans. Image Process.*, vol. 27, no. 1, pp. 106–120, Jan. 2018.
[48] M. J. Fadili, J.-L. Starck, J. Bobin, and Y. Moudden, "Image decomposition and separation using sparse representations: An overview," *Proc. IEEE*, vol. 98, no. 6, pp. 983–994, Jun. 2010.
[49] J. Rapin, J. Bobin, A. Larue, and J.-L. Starck, "Sparse and non-negative BSS for noisy data," *IEEE Trans. Signal Process.*, vol. 61, no. 22, pp. 5620–5632, Nov. 2013.
[50] D. Heinz and C.-I. Chang, "Fully constrained least squares linear mixture analysis for material quantification in hyperspectral imagery," *IEEE Trans. Geosci. Remote Sens.*, vol. 39, no. 3, pp. 529–545, Mar. 2001.
[51] D. D. Lee and H. S. Seung, "Algorithms for non-negative matrix factorization," in *Proc. Adv. Neural Inf. Process. Syst.*, 2001, vol. 13, no. 1, pp. 556–562.
[52] M. W. Berry, M. Browne, A. N. Langville, V. P. Pauca, and R. J. Plemmons, "Algorithms and applications for approximate nonnegative matrix factorization," *Comput. Statist. Data Anal.*, vol. 52, no. 1, pp. 155–173, 2007.
[53] P. Paatero and U. Tapper, "Positive matrix factorization: A non-negative factor model with optimal utilization of error estimates of data values," *Environmetrics*, vol. 5, no. 2, pp. 111–126, 1994.
[54] A. Cichocki, R. Zdunek, and S.-I. Amari, "Hierarchical ALS algorithms for nonnegative matrix and 3D tensor factorization," in *Proc. Int. Conf. Independ. Compon. Anal. Signal Separat.*, vol. 4666, 2007, pp. 169–176.
[55] J. Bobin, Y. Moudden, J. L. Starck, and M. Elad, "Morphological diversity and source separation," *IEEE Signal Process. Lett.*, vol. 13, no. 7, pp. 409–412, Jul. 2006.
[56] J. Bobin, J.-L. Starck, J. M. Fadili, Y. Moudden, and D. L. Donoho, "Morphological component analysis: An adaptive thresholding strategy," *IEEE Trans. Image Process.*, vol. 16, no. 11, pp. 2675–2681, Nov. 2007.
[57] E. Candès, L. Demanet, D. Donoho, and L. Ying, "Fast discrete curvelet transforms," *Multiscale Model. Simul.*, vol. 5, no. 3, pp. 861–899, 2006.
[58] P. L. Combettes and V. R. Wajs, "Signal recovery by proximal forward-backward splitting," *Multiscale Model. Simul.*, vol. 4, no. 4, pp. 1168–1200, 2005.
[59] J. M. Bioucas-Dias and J. M. P. Nascimento, "Hyperspectral subspace identification," *IEEE Trans. Geosci. Remote Sens.*, vol. 46, no. 8, pp. 2435–2445, Aug. 2008.